

Mechanics of a granular *skin*

Somnath Karmakar, Anit Sane, S. Bhattacharya and Shankar Ghosh

Department of Condensed Matter Physics and Materials Science,
Tata Institute of Fundamental Research, Homi Bhabha Road, Mumbai 400005, India

(Dated: October 16, 2018)

Magic Sand, a hydrophobic toy granular material, is widely used in popular science instructions because of its non-intuitive mechanical properties. A detailed study of the failure of an underwater column of magic sand shows that these properties can be traced to a single phenomenon: the system self-generates a cohesive *skin* that encapsulates the material inside. The *skin*, consists of pinned air-water-grain interfaces, shows multi-scale mechanical properties: they range from contact-line dynamics in the intra-grain roughness scale, plastic flow at the grain scale, all the way to the sample-scale mechanical responses. With decreasing rigidity of the *skin*, the failure mode transforms from brittle to ductile (both of which are collective in nature) to a complete disintegration at the single grain scale.

INTRODUCTION

Dry granular systems are known to exhibit both liquid and solid-like properties. While there are many instances where a granular assembly exhibits liquid-like properties [1–4], examples of granular systems illustrating solid-like properties are rare with one exception: the typical conical sandpile shape [5]. To craft more complex shapes, e.g., sand art, it is necessary to add additional constraints. These constraints can be added in the bulk or at the boundary. Adding a small quantity of water to the sand introduces constraints in the bulk in the form of capillary bridges [6–9]. Conversely, encapsulating dry grains in a container is an example of constraints that are applied at the boundary [10].

In general, encapsulation requires isolating materials from their surroundings and it is achieved either by (i) introducing another material in the interfacial region or (ii) facilitating processes at the interface that create self-encapsulation. Examples of the former range from the simple instance of a bag or a silo containing cereal grains to more complex examples of thin polymer films wrapping liquid droplets [11, 12], texturing of liquid droplets (‘liquid marbles’) by attaching hydrophobic powder to its surface [13] and stabilizing emulsions by particles or surfactants [14, 15]. In contrast, a liquid that oxidizes on contact with atmosphere to develop a stress bearing skin is an example of self-encapsulation [16].

In this paper we study the self-encapsulation of a granular system consisting of hydrophobic sand [17–20] under water. This system self-generates a *skin* which encapsulates dry hydrophobic sand-grains and stabilizes the trapped air (bubble) against the force of buoyancy. Removal of trapped air breaks down this encapsulation. The paper also explores the mechanical properties of this system at multiple scales: from the pinning of the three phase contact line at the roughness scale of the particle, plastic flow at the grain-scale, to sample-spanning mechanical responses. It may be noted here that while hydrophilic granular systems – both dry and wet – are

widely studied [5, 21], hydrophobic sand grains submerged in a non-wetting liquid like water remain largely unexplored [17–20] even though such systems are of practical importance, especially in pharmaceutical, food and petroleum industries where newer encapsulation strategies are in great demand [22].

Mechanical response of a system is usually described in a small neighborhood of a reference state. For a dry granular assembly a ‘state’ of a system is described in terms of the center of mass of the grains and the forces among them. For values of strain smaller than 10^{-5} , dry granular assemblies show elastic response, i.e., the reference state can be restored by setting the applied forces to zero (see p 92 of [23]). This elastic response comes from the reversible deformation of the region of contact between the grains. However, to describe the state of the hydrophobic sand immersed in water the information regarding the center of mass of the grains is not sufficient. We need to augment it with additional information about the detailed layout of the three phase contact lines and the local contact angles of the *skin*. The three phase contact lines formed at the grain-water-air interface are immobilized (pinned) by defects present in the system [24–26]. Any additional deformation of the *skin* causes the contact angles to change from their reference values. This generates restoring forces in the system, i.e., if the contact angle changes from θ to θ^d the restoring force per unit length is $\simeq \gamma(\cos \theta^d - \cos \theta)$, here γ is the surface energy at the water-air interface. The pinning and depinning of these contact lines determine the mechanical properties of the material and its mode of failure. Hence, the present study is an example of the more general problem of studying statics and dynamics of systems with elastic interfaces in a random environment [27].

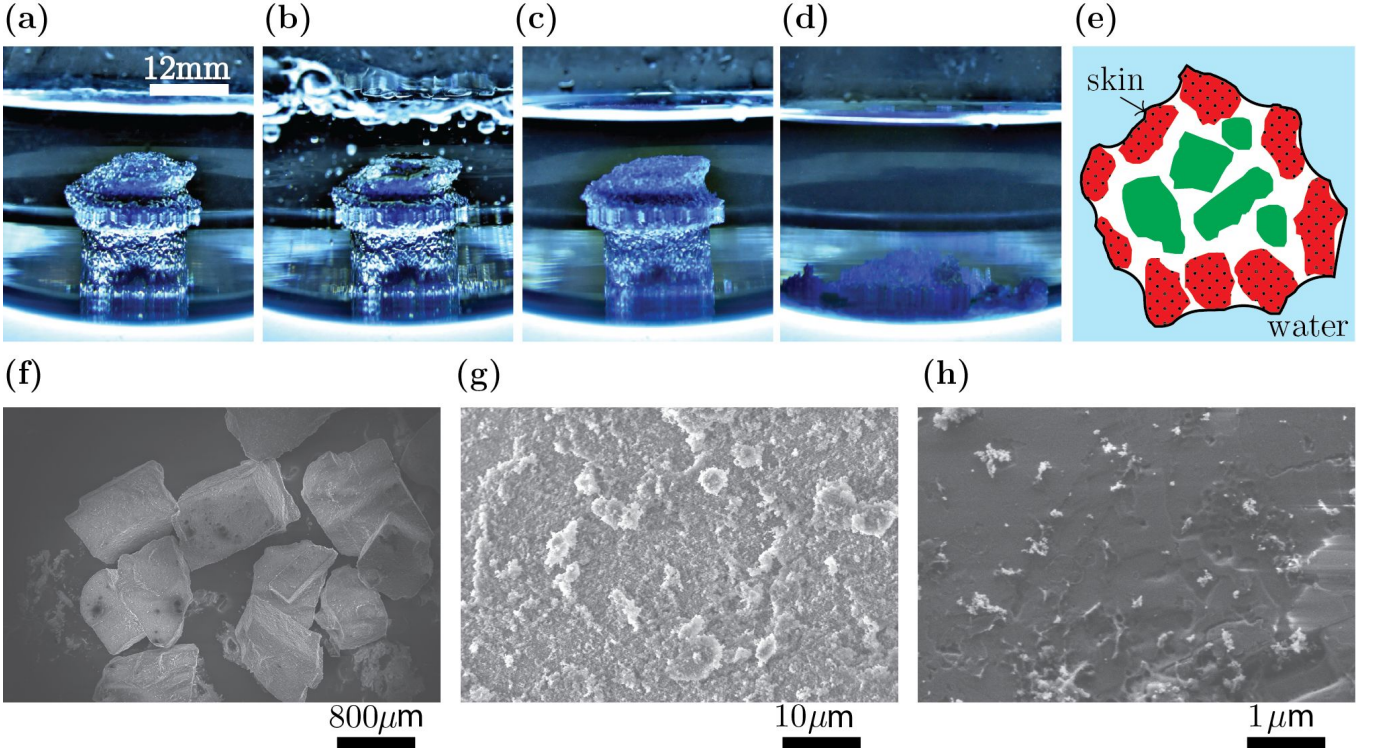


FIG. 1. Image (a) shows an underwater lump-like rigid structure when magic sand is poured into water. The lump has luster on its surfaces caused by total internal reflection of light at the air-liquid interfaces. When air is gradually removed by pumping (see (b)) the lump loses its luster (as seen in (c)). This luster-less lump, when mechanically perturbed, disintegrates into a shallow flat bed (see (d)). A cross-sectional top-view of the lump in (a) which is schematically shown in (e), captures the liquid shapes at the ‘grain-water-air’ interfaces. The grains that reside on the lustrous *skin* are marked in red (with dots) and the dry grains in the interior are marked in green; the water and air phases are coloured in blue and white, respectively. Note, that the *skin* supports the weight of the interior dry grains and is hence under tension. The panels (f) and (g) show the scanning electron micrographs of the sand grains for two different values of magnification. The grain surfaces are decorated with micron-sized hydrophobic patches. Washing hydrophobic sand in acetone removes the surface patches and makes the material hydrophilic. The micrograph of the acetone-washed sand grain is shown in panel (h).

THE HYDROPHOBIC GRAINS AND THEIR WETTING PROPERTIES

As hydrophobic granular material, we use polyhedral shaped ‘Magic Sand’ grains sourced from Education Innovation Inc. (USA). They are made by coating polyhedral shaped sand grains with a hydrophobic material. Alternatively, these hydrophobic particles can be made in the laboratory by coating similar sand particles with FluoroPel PFC from Cytonix LLC silica [28].

When grains of magic sand are freely poured into water, they spontaneously form a cohesive lump: a typical example of which is shown in Fig.1(a). The immediately evident features are: (i) the system retains its shape and (ii) the outer surface of the lump has a luster that originates from the total internal reflections of light at the pinned water-air interface [29, 30]. On degassing of the system achieved by creating a partial vacuum over the liquid (Fig.1(b)), the lump begins to lose its luster (Fig.1(c)) and when this luster-free system is mechanically perturbed, it slumps to form a flat sand-bed inside wa-

ter (Fig.1(d)). A cross-sectional top-view of the granular lump in Fig.1(a) is schematically shown in Fig.1(e). The grains (red coloured with dots) on the boundary together with the pinned water-interface constitute an encapsulating granular *skin* which provides the submerged lump its structural integrity. The force of buoyancy of the trapped air and the weight of dry sand grains in the interior (coloured with green) exerts stress on the *skin* causing it to be under tension.

The scanning electron micrographs of the grain surface are shown in Fig.1(f) and (g), for two different values of magnification. The micron-sized rough patches (see Fig.1(g)) which come from the hydrophobic coating on the particle surface are crucial for the observed wetting properties of these sand grains [25]. The equilibrium contact angle is measured to be about 150° for a $\approx 50 \mu\text{L}$ water drop placed on a single hydrophobic grain (see Fig.2(a)). For the same droplet in a tilted configuration, the advancing and receding contact angles are found to be $\approx 170^\circ$ and $\approx 120^\circ$ respectively, i.e., the contact angle hysteresis is $\approx 50^\circ$; see Fig.2(b). The higher magni-

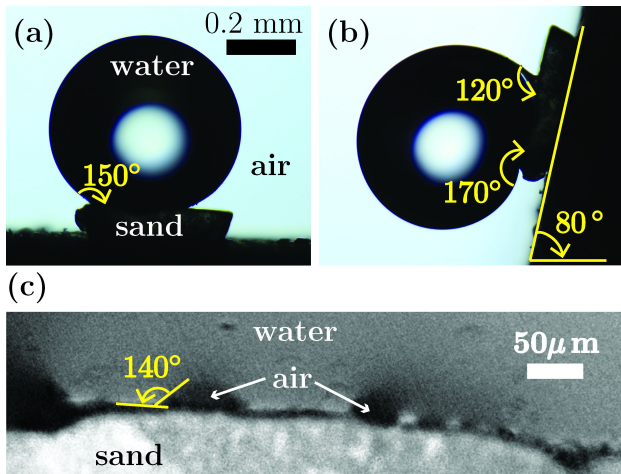


FIG. 2. (a) Equilibrium contact angle of $\approx 150^\circ$ obtained for a water-drop ($\approx 50\mu\text{L}$) placed on a single hydrophobic grain surface. (b) Advancing and receding contact angles are measured to be $\approx 170^\circ$ and 120° respectively, for the same water droplet in a tilted configuration. (c) Existence of isolated air bubbles on the topographic grain surface viewed at a larger magnification.

figuration image of water-grain interface in Fig.2(c) shows presence of small isolated air bubbles trapped between the grain and the water which have similar equilibrium contact angles ($\approx 140^\circ$), i.e., the surrounding water is in partial contact with the hydrophobic sand grains which creates a Wenzel type wetting scenario [25, 26]. Washing these grains in acetone removes the hydrophobic coating and exposes the underlying smooth hydrophilic surface (Fig.1(h)).

CONSTRUCTION OF A SUBMERGED FREE-STANDING COLUMN

In order to obtain a more comprehensive understanding of the mechanical properties of the system, we choose a relatively simple geometry which is a free-standing submerged cylindrical column built with magic-sand, using the following experimental steps. At First, by selective sieving we obtain grains of different mean sizes a , ranging from $250\mu\text{m}$ to 2mm . Second, an acrylic tube of inner diameter d is made to rest vertically on the flat base of an empty rectangular glass container. The grains are thereafter gently poured into the tube upto a desired height L_0 . This forms a *wall-supported* granular column shown in the left panel of Fig.3(b). The typical packing fraction ϕ of the grain assembly is about 0.53. Third, and in a key step, the acrylic tube is gradually pulled out while simultaneously filling the glass container with water. Consequently, the hydrostatic pressure partially compensates for the over-pressure due to weight of the grains. This unique protocol prevents grains from clog-

ging

Particles which are in constant physical contact with the wall of the acrylic tube are immobilized by the frictional interactions. As the tube is withdrawn, it drags along particles that are in contact with it. This exposes the next layer of particles to water, on which the *skin* forms. The resulting particle rearrangements reduce the diameter by $\approx 1\%$ and increase the height of the column which is now partially submerged in water by ΔL . The radial contraction happens within the first few seconds and does not evolve appreciably over time. However, the axial strain $\Delta L/L_0$ keeps increasing in time; see Fig.3(c). As the tube is pulled out, the number of sand grains which are in contact with it decreases. This reduces the extent of particle rearrangements. As a result, the rate of change of ΔL decreases with time. The fully submerged column has a length L which is about $\approx 9\%$ larger than the initial length L_0 of the wall-supported column. Hence, the volume fraction of the submerged column is about 7% lower than its value for the wall-supported case. This free-standing submerged column is shown in the middle panel of Fig.3(b). The column is anchored via capillary forces with the hydrophobic substrate at the bottom and is slightly flared close to the anchoring region. Under an identical protocol, hydrophilic beach sand instead slumps to form a canonical sandpile [31].

MECHANICAL PROPERTIES OF THE COLUMN

The submerged column can be thought of as a thin cylindrical shell (made from the *skin*) containing non cohesive dry grains in its interior. The *skin* is about a particle diameter thick and it comprises of the sand grains on the outer surface of the column and the pinned three phase contact line. Using a Du-Noüy ring based technique [32] we measure the interfacial energy of the *skin* to be about 0.05N/m . At a microscopic scale this interfacial energy arises from the pinning of the three phase contact line to the defects present on the surface of the grains (see Fig. 2(c) [24]. The cohesive coupling stiffness \mathcal{K} due to this pinning depends on the size of the defect ℓ_{dis} and the typical separation ζ between them. In the limit of strong but sparsely distributed defects, $\mathcal{K} = \pi\gamma/(\ln(\zeta/\ell_{dis}))$, where γ is the surface energy at the water-air interface [33]. Experimentally we observe that polyhedral grains with smooth coverage of hydrophobic coating consistently fail to sustain submerged columns. This suggests that of the multiple scales present in the system, the micron-sized hydrophobic patches present on the surface of the grains are most effective in pinning the contact line.

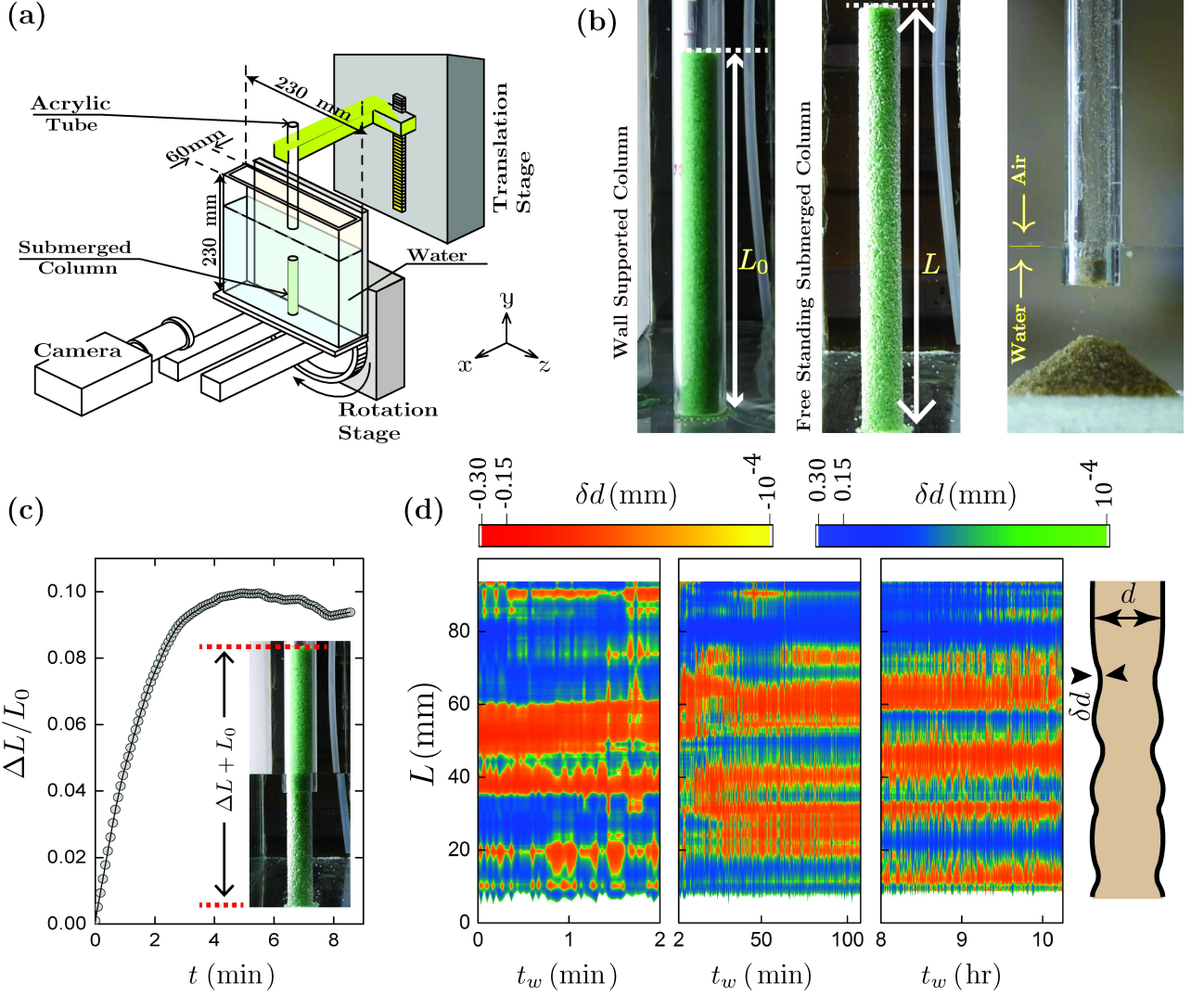


FIG. 3. (a) Schematic of the experimental setup to study the mechanical response of sand columns in the presence of body forces. The vertical water-filled glass container, mounted on a rotary stage, is gradually tilted to apply body forces to the column. (b) Images of a *wall-supported* (left panel) and a submerged hydrophobic sand columns (middle panel). The right panel contrasts the response of hydrophilic sand in water that slumps to form a sand pile. (c) Axial strain $\Delta L/L_0$ as a function of time t while the column is being made; Inset: column preparation at an instance time. (d) The contour plots show time evolution of the changes in the diameter δd from its mean value for the submerged column ($d = 11$ mm, $a = 500$ μ m) along its vertical length L . The blue and the orange bands correspond to regions with positive ($\delta d > 0$) and negative ($\delta d < 0$) modulations of the diameter, respectively. The right-most panel shows a schematic representation of the peristaltic modulations created by the wrinkles on the *skin*.

Growth of imperfections of the column

The process of making the column introduces localized geometric imperfections which evolve slowly in time. This is captured by the contour plots of the variation δd of the column diameter from its mean value along its length over four orders of magnitude in waiting time t_w (Fig.3(d)). In Fig.3(d) the blue regions correspond to regions with positive, $\delta d > 0$, modulation and the orange regions correspond to regions with negative, $\delta d < 0$, modulation. The maximum δd is found to be around 0.3 mm,

nearly half-a-particle size a ; whereas the width of the modulation in d along L is much larger, approximately 40 particle-lengths. The slow temporal evolution of the column's deformation is indicative of creep in the presence of strong inter-grain friction, brought about by the competition between the stresses exerted on the *skin* by the dry grains in the interior [10] and the interfacial energy density of the *skin*. Henceforth, we refer to it as the wrinkling of the *skin*.

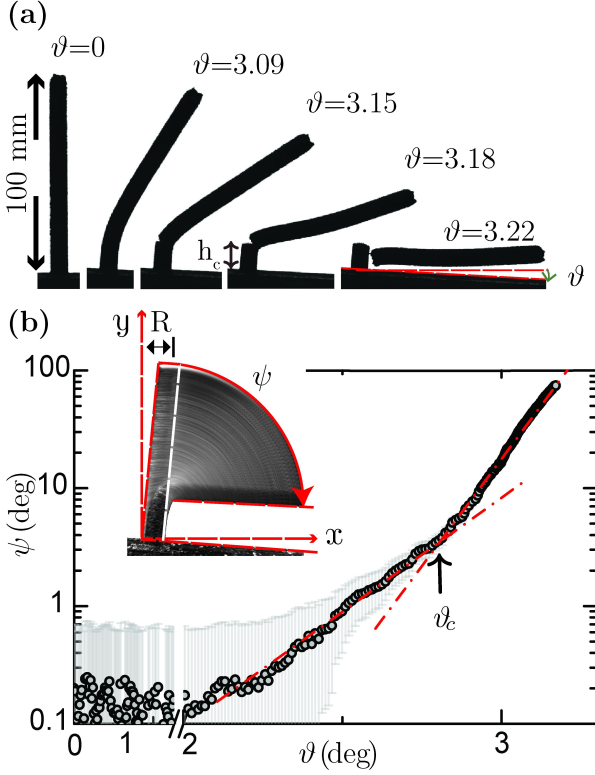


FIG. 4. (a) The figure shows sequence of images for increasing tilt angle ϑ which captures the mechanical failure of the submerged column. Note that unlike the case of a “falling chimney” which breaks *backward* in mid-air [34, 35] the submerged column breaks *forward* (with the exception of a slight catenary shape seen towards the top for $\vartheta = 3.18$). (b) Variation of the failure angle ψ on the tilt angle ϑ (protocol of continuous tilting). Beyond the critical tilt angle ϑ_c the variation of ψ with ϑ changes its slope on a semi-log plot (shown by the red colored dash-dotted lines). The inset shows the overlay of the images for falling of the column; where R is the distance of the mid-point of the top of the column from the point $(0, L)$ on the y -axis.

An order of magnitude estimate of the elastic constant

In this section we make an order of magnitude estimation of an effective elastic constant for the column. To do so, we apply increasing body forces to the column by gradually tilting the vertical water-filled glass container at a fixed rate; for experimental details see Fig.3(a). Fig.4(a) displays five representative images of the column for increasing values of the tilt angle ϑ made by the base of the container with respect to the horizontal. Images corresponding to $\vartheta = 3.15^\circ$ and $\vartheta = 3.18^\circ$ capture the process of the column breaking which resembles a mode-I type transverse rupture. As the column breaks from a finite column height h_c , its upper-part traces out a distinct arc, $y \simeq h_c \cos \vartheta + L_\psi \cos \psi \cos \vartheta$ (the inset of

Fig.4(b). Here ψ is the failure angle made by the axis of the falling part with a line whose slope is $\cot \vartheta$ and L_ψ is the length of the falling part of the column. The column for $\vartheta = 3.15$ is about 3% longer than its length for $\vartheta = 0$. The variation of failure angle ψ with ϑ changes slope at ϑ_c in a semi-log plot (see Fig.4(b)). The large slope beyond ϑ_c indicates a rapid toppling of the upper part of the column. We use ϑ_c to mark the onset of mechanical failure. The broken part of the column sinks as a single object.

One cannot build an arbitrarily long and/or thin column. If the gravitational energy $\simeq A(\rho - \rho_f)\phi gL$ of the column exceeds its bending energy $\simeq \frac{YI}{L^2}$, the column will break, here Y is the effective Young’s Modulus of the column, $A = \frac{1}{4}\pi d^2$ is its cross sectional area, $I = A^2/2\pi$ is moment of inertia of the column and ρ and ρ_f are the densities of sand and water, respectively. To estimate the maximum height L_m of a column we equate the gravitational energy to the bending energy to obtain,

$$\left(\frac{d^{2/3}}{L_m}\right) = \left(\frac{(\rho - \rho_f)\phi g}{Y}\right)^{1/3}.$$

At this maximum height the column breaks in its upright position, i.e., $\vartheta_c = 0$; this allows us to construct an alternative estimate of L_m from the experimentally observed linear variation $\tan \vartheta_c = -c_0 + \left(\frac{\ell_\vartheta d^2}{L^3}\right)^{1/3}$ where $c_0 \approx 0.15$ and $\ell_\vartheta \approx 0.12$ m are fitting parameters; see Fig.5(a). For $\vartheta_c = 0$, we obtain

$$\left(\frac{d^{2/3}}{L_m}\right) = \left(\frac{c_0^3}{\ell_\vartheta}\right)^{1/3}.$$

For $d = 11$ mm, $L_m = \left(\frac{\ell_\vartheta d^2}{c_0^3}\right)^{1/3} \approx 0.16$ m. This estimate of L_m is consistent with experimental observations that stable 11 mm diameter columns could only be built to the height of ≈ 0.15 m. Columns built greater than this height are unstable and fail in their upright position. Equating the above two expressions for $\left(\frac{d^{2/3}}{L_m}\right)$ we obtain $Y \simeq \phi g(\rho - \rho_f)(\ell_\vartheta/c_0^3) \approx 10^5$ Pa for the submerged column. This is about two orders of magnitude smaller than that observed for wet sand containing 1% water by volume [36].

Heuristic arguments for calculating h_c : The falling column is visually similar to the well studied problem of a “falling chimney” that breaks mid-air due to tilting [34, 35]. For the case of a falling chimney the tensile stress at the leading-edge and the compressive stress at the trailing-edge at small tilt angles is maximum at $\sim L/2$ (for tilt angles greater than 45° it is about $L/3$), and is usually the point from where the chimney fails [34]. Though, one expects a similar spatial variation of the stress for the submerged column, when $L < L_m$, we find the following (i) the height h_c at which the column breaks varies quadratically with the column length L ;

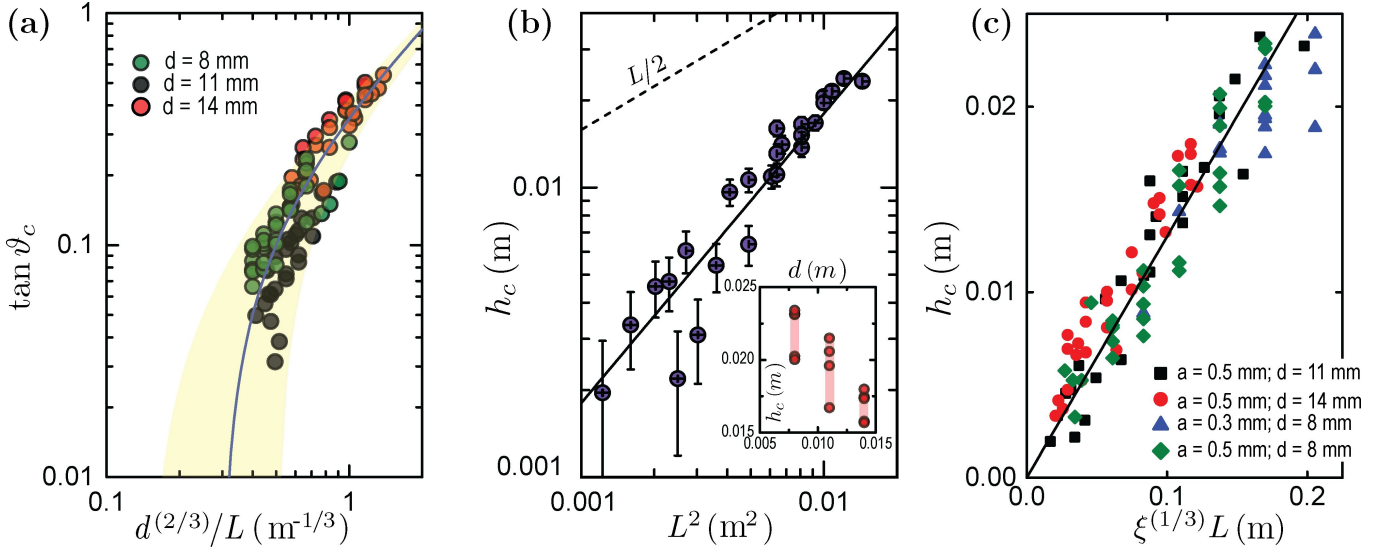


FIG. 5. (a): Variation of $\tan \vartheta_c$ as a function of $d^{2/3}/L$. The solid line is a numerical fit for the expression: $\tan \vartheta_c \simeq -c_0 + (\frac{\ell_\vartheta d^2}{L^3})^{\frac{1}{3}}$ where $c_0 \approx 0.15$ and $\ell_\vartheta \approx 0.12$ m are obtained from fitting. The confidence band of the fitting is marked in yellow. (b) Variation of h_c as a function of L^2 , obtained for $d = 11$ mm and $a = 500$ μ m. The solid line is a linear fit of $h_c = L^2/\ell_\beta$, where $\ell_\beta \approx 0.5$ m. The inset shows the variation of h_c as a function of d , obtained for $L = 100$ mm and $a = 0.5$ mm. For a contrast, the dashed line $h_c = L/2$ corresponds to the failure criteria of the chimney's falling for small tilt angles [34]. (c): Variation of h_c with $\xi^{1/3}L$ for submerged columns of different d 's, a 's and L 's. The solid line shows the linear dependence.

see Fig.5(b) and (ii) h_c decreases with increasing column diameter; see the inset of Fig.5(b).

From a dimensional argument, for values of L smaller than L_m , we propose that the height h_c is related to the column length L by the following relation $h_c = f(\xi)L$ where $\xi = A\phi g(\rho - \rho_f)L^3/YI = 8\phi g(\rho - \rho_f)L^3/Yd^2$ is the ratio of the gravitational and the bending energies [37]. Since $h_c \propto L^2$, $f(\xi)$ must vary as $\xi^{\frac{1}{3}}$, i.e.,

$$h_c \propto \xi^{1/3}L.$$

A good agreement of this expression with a large set of experimental data, obtained for different lengths and diameters of the submerged column and for various grain sizes, are shown in Fig.5(c). Here, we have taken the effective Young's modulus of the column $Y (= 10^5$ Pa) to be a constant, independent of the grain scale, which implies an approximate validity of a continuum mechanical description of the system in this range of deformation.

The connection between the wrinkling of the *skin* and the critical height h_c

The functional dependence of the critical buckling stress on the geometrical parameters for a cylindrical column is different from that of a cylindrical shell. For the column the critical stress is proportional to $(d/L)^2$ [38] whereas for a shell it is proportional to (a_δ/d) [38]. Here a_δ is the thickness of the shell. In the present experiments $(d/L) \approx 0.1$ and $(a_\delta/d) \approx 0.005$, where the shell

thickness a_δ is of the order of particle diameter ≈ 0.5 mm. Thus, there are two critical stress values; one that corresponds to the buckling of the shell (*skin*) and the other that corresponds to the buckling of the column. Since $(d/L)^2 > (a_\delta/d)$, for increasing values of stress, the buck-

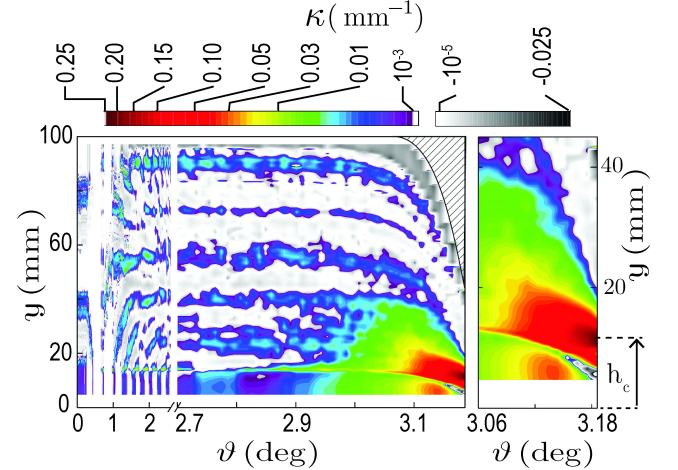


FIG. 6. Left panel: Contour plot of the curvature κ along y -axis for varying ϑ . The curvature data is calculated for the advancing (right) edge. The column can take in any value within the range $\{0, y_{max}\}$ on the y axis. When $\vartheta = 0$ the maximum projected height of the column on the y axis equals the total length of the column, i.e., $y_{max} = L$. As the column tilts y_{max} decreases. The hatched region corresponds to the values on the y axis where $y > y_{max}$. Right panel: zoomed-in portion of this same plot at close to the failure height h_c .

ling of the shell which causes the *skin* to wrinkle, precedes the failure of the column (assuming that the elastic constant of the entire column is greater than or equal to the elastic constant of the *skin* alone).

The *skin* is an integral part of the column and its wrinkling influences the buckling of the column in the following way. The wrinkles on the *skin* generates geometric imperfections of the column. These imperfections (i) lowers the critical stress at which the system fails [39] and (ii) influence the location from where the system fails. To study the role played by the wrinkles (geometric imperfections of the column) in determining the height h_c from which the column fails we track the curvature κ of the column along its length for the leading edge till the column breaks up into two pieces.

To calculate κ , the boundaries of the leading and the trailing edges are passed through a low pass filter that suppresses features smaller than a single grain size [40]. These edges are detected using an edge detection algorithm based on [41]. Fig.6 shows the curvature data for the advancing edge.

The contour plot of the curvature clearly shows the existence of bands of high curvature along the length of the column. These bands correspond to the wrinkling of the *skin* (Fig.3(d)). As the column tilts the lowest wrinkle develops into the most prominent imperfection of the column and it acts as a seed from where the failure of the column is initiated.

The critical height h_c from where the column breaks varies quadratically with the length L of the column. Since the location of the lowest wrinkle coincides with h_c , it is natural to expect the wavelength associated with the wrinkles to have the same L dependence as h_c . However, within the framework of shell buckling, the wavelength of wrinkles is independent of the length of the column [38]. So, a model based solely on buckling produced by static loading is inadequate to describe the experimental scenario.

We speculate that the observed length dependence of h_c is related to the perturbations imparted to the column by the mechanical noise associated with the process of tilting. This gives the loading a certain dynamic character which could in principle facilitate coupling of the various global length-dependent buckling modes to the wrinkling induced localized imperfections of the column [42, 43]. This conjecture needs to be examined in future in greater detail.

Opening of the wedge between the falling top and the anchored bottom of the column

The inset image in Fig.7 displays an instantaneous distance D at the apex of the *visually identified wedge* between the falling top and the anchored bottom parts of the column. This wedge opens up from the trailing (left)

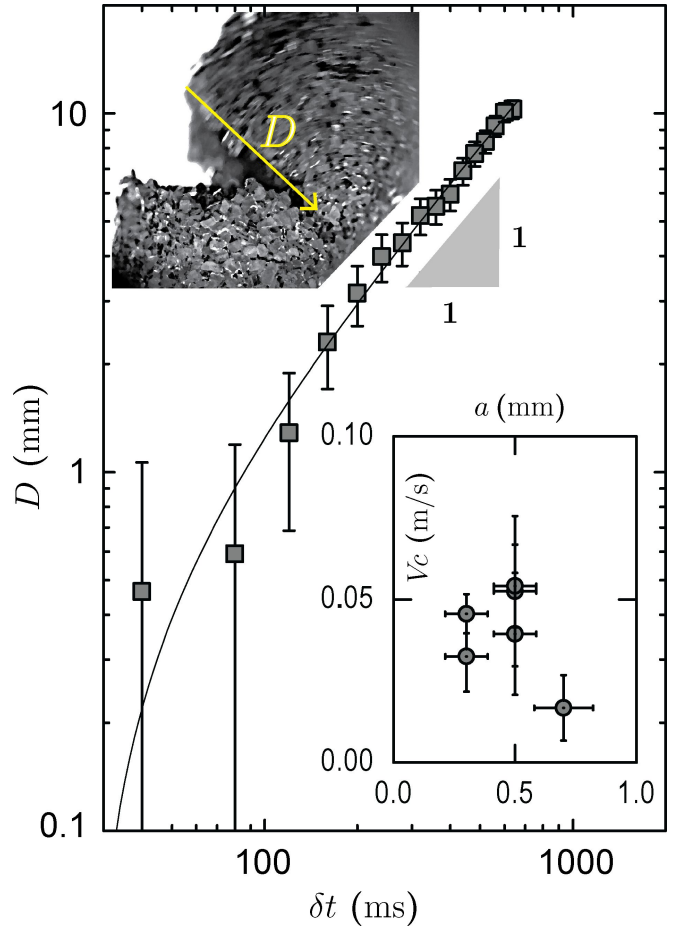


FIG. 7. Progression of the wedge length D (marked in the inset image) as a function of the time δt measured onwards from the first observable instance of the wedge opening at the left edge between the falling top and the anchored bottom. The lower inset shows the variation of the velocity V_c at which the breaking front progresses with the grain size a .

edge and progresses towards the advancing (right) edge of the column. The variation of this distance D with time δt is plotted in Fig.7, here the time δt is measured onwards from the first observable instance of the wedge opening at the left edge between the falling top and the anchored bottom. As can be seen, the wedge advances with an average velocity of $V_c \approx 0.02$ m/s.

Neglecting the viscous drag, the time required for a non-anchored column to topple can be obtained by equating the toppling torque acting through the center of mass of the falling part of the column and the rate of change of the angular momentum. This ‘shortest’ falling time is about a second which is the same for the wedge to move across the sample. Accounting for the viscous drag will increase the estimate of the falling time. Unlike conventional solids which break by developing cavities in the bulk, the interior of the submerged column is made of dry grains that cannot support an open gap. The gap can be sustained only if water drains in and generates a confin-

ing *skin* which prevents individual particles from falling into it. Hence, the speed at which the wedge opens sets a lower limit on the tearing speed of the *skin*. The inset of Fig.7 shows that the particle size influences the speed V_c at which the apex of the visually identified wedge between the falling top and the anchored bottom moves – suggesting that the wedge opening is influenced by tearing of the *skin*.

Effect of stress cycling on the *skin*

Figure 4 (a) shows that tilting of the column alters the shape of the column. To study the elastic and plastic response of the column, we utilize an incremental stress-cycling protocol; which is the mechanical equivalent of minor hysteresis loop in magnets [44]. Here, the column is recursively stressed such that the minor loops have three branches: (i) an increase- ϑ branch where the tilt angle increases from 0 to ϑ_n^m at a fixed rate (ii) a clamp- ϑ branch where the tilt angle is held constant at ϑ_n^m for a fixed period of clamping time and (iii) a decrease- ϑ branch which corresponds to decreasing the tilt angle from ϑ_n^m to 0, with the same rate as in (i). They are accessed sequentially. For each successive cycle, the maximum tilt angle ϑ_n^m increases linearly with n , where n is the numerical index for the cycle. An instantaneous configuration of the submerged column is referred to as $\mathcal{C}(n, \vartheta : \tau)$, where τ is the time spent by the system in the clamped state. Fig.8A shows the cyclic variation in the relative displacement $(\varepsilon - \sin \vartheta)$ as a function of the tilt angle ϑ for selective values of $n = 1, 7, 11$ and 13 respectively; here $\varepsilon = R/L$ and R is the distance of the mid-point of the top of the column from the point $(0, L)$ on the y -axis (the inset of Fig.4(b)). For a first few cycles ($n \leq 5$), i.e., for smaller values of ϑ_n^m , the *skin* deforms in a reversible manner. We limit our statement of the reversibility: it is entirely possible that while the *skin* may behave in a reversible manner, the dry grains in the interior of the column may not. For larger values of ϑ_n^m ($n > 5$), the column shows noticeable irreversibility and hence, the hysteresis increases. The parameter $(\Delta\varepsilon_n - \sin \vartheta_n^m)$ is a measure of the strain developed in each cycle while the parameter Ω determines the loop area of each stress cycle; which is a measure of the accumulated hysteresis and dissipation in the system, here $\Delta\varepsilon_n = \varepsilon|_{\vartheta=0} - \varepsilon|_{\vartheta=\vartheta_n^m}$. The top and bottom panels of Fig.8B show variation of these two parameters as a function of the maximum tilt angle ϑ_n^m , respectively.

The following observations can be made from Fig.8 (a) and (b) : (i) the elastic regime of the column extends for $\vartheta_n^m = 1.5^\circ$ beyond which the area of the hysteresis loop Ω begins to increase abruptly. This elastic regime (non-shaded region of Fig. 8(b) can accommodate strains of the order of 5×10^{-3} which is much larger than that observed for dry granular systems. (ii) In the elastic

regime, the recursive stress cycling shows smooth variation in $(\varepsilon - \sin \vartheta)$ with ϑ . However, beyond the elastic regime ($n > 5$ or $\vartheta_n^m > 1.5^\circ$, the shaded region of Fig. 8(b) this variation becomes increasing jagged and clearly shows discrete ‘jumps’ interspersed with smoothly varying sections. These jumps are signatures of mechanical instabilities associated with contact line slippages. They are related to the stress (tilt) induced reduction of the energy barriers associated with the underlying pinning potential which allows the ambient noise (fluctuations) to induce creep like motion of the contact line. Anomalies of elastic constants associated with the break down of linear elastic response generates similar jumps in the flow curves of disordered materials [45, 46]. (iii) The maximum size of the jump height seen in the quantity $(\varepsilon - \sin \vartheta)$ is about $0.01 \approx \mathcal{O}(a/L)$, i.e., the contact line on an average moves by a particle scale. Further motion of the contact line is possible only by jumping to the next grain which is restricted by the presence of sharp edges at the grain corners [47]. (iv) The increase in Ω is caused by the cumulative effects of these jumps. These jumps progressively generate local overhangs along the direction of the tilt. This results in the column breaking forward unlike a rigid “falling chimney” which breaks backward [34, 35].

The effects of stress assisted creep are best seen in the deformation of the column for the various clamp – ϑ branches (here ϑ is held constant at ϑ_n^m , see Fig.8(c)). The creep increases with increasing tilt angles (forces), e.g., see the $n = 14$ branch in Fig.8(c). Even during creep the column evolves in a similarly punctuated stick-slip manner with jumps in the quantity $(\varepsilon - \sin \vartheta)$ being limited by the value a/L .

As the occurrences of creep increase, the survival–time τ_{surv} of a stationary stick phase decreases; see the inset of Fig.8(c). The jumps themselves are abrupt in the experimental time scale: they occur over a period less than 10 ms, an order of magnitude shorter than the measured shortest survival time (100 ms). The breaking of the column at the macroscopic scale (see Fig.7) is visible only for values of τ greater than 10 s. This region shows a rapid growth of $(\varepsilon - \sin \vartheta)$, its initiation is marked by an arrow in Fig.8(c).

BRITTLE TO DUCTILE TO A SINGLE PARTICLE DISINTEGRATION: TUNING THE FAILURE MODE

These results imply that the *skin*, comprising of the air-water-grain interface on the surface layer of grains, is primarily responsible for the mechanical response of the entire system and any modification of the *skin* will modify the behaviour of the system. One striking modification is shown in Fig.9 where we create a partial vacuum over the water surface, so that the trapped air within

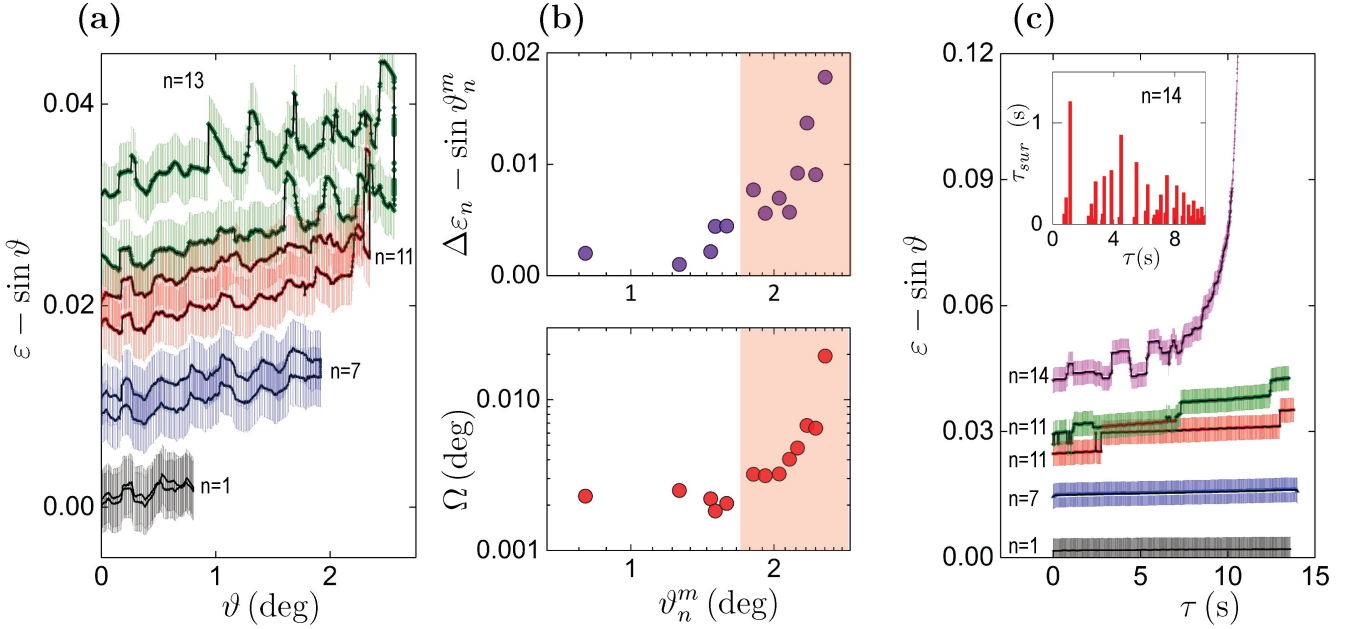


FIG. 8. (a) Variation of $(\varepsilon - \sin \vartheta)$ as a function of the tilt angle ϑ for the entire collection of selective minor-loops, where $\varepsilon = R/L$. Here, R is the distance of the mid-point of the top of the column from the point $(0, L)$ on the y -axis. (b) In top and bottom panels, the strain $(\Delta \varepsilon_n - \sin \vartheta_n^m)$ and total area under the hysteresis loop Ω are plotted as a function of increasing ϑ_n^m , respectively. Here, $\Delta \varepsilon_n = \varepsilon|_{\vartheta=0} - \varepsilon|_{\vartheta=\vartheta_n^m}$. The shaded region is dominated by plastic response. (c) Variation of $(\varepsilon - \sin \vartheta)$ as a function of clamp time τ for different values of n in the *clamp*- ϑ branch for $n = 1, 7, 11, 13$ and 14 . The inset shows variation of the survival time τ_{surv} of a state of the column as a function of τ for $\mathcal{C}(n = 14, \vartheta = 2.6^\circ, \tau < 10 \text{ s})$. The data shown here are for a column whose $L = 100 \text{ mm}$, $a = 500 \mu\text{m}$, $d = 11 \text{ mm}$.

the column, one key component of the *skin*, escapes out from the system as bubbles. The time-lapsed images in Fig.9 (a) \rightarrow (e) demonstrate that here too the failure is initiated by bending at a finite critical height. But, in contrast to the single tear shown above, the column shows large-scale plastic deformations. Its structural integrity is extended for values of ψ greater than 90° by forming a deformed neck, i.e., a narrowing of the column's diameter, instead of forming a tear or a crack as above. Here, the failure proceeds via this necking instability whose spatial location is marked by an arrow in Fig.9(e). Such large-scale (many-grains wide, in this case) plastic flow and necking instabilities are typical of ductile mode of failure in solids [48], in complete contrast with the brittle failure described above. This change in failure-mode is brought about by the loss of entrapped air causing weaker cohesion in the column that results in conformational changes of a softer *skin* and finally leads to the ductile failure of the column.

For completeness, we note that a third, and limiting, mode of failure occurs if degassing continues for a long time. In the absence of air, the *skin* begins to lose its strength (see the lustre-less lump in Fig.1(c)). The weak *skin* eventually fails to sustain the inward hydrostatic pressure and slumps under the slightest mechanical disturbance. The water quickly drains in as the structure disintegrates into a heap of particles, seen in

both Fig.1(d) and Fig.9(f); the hydrophobic sand then behaves like its hydrophilic counterpart (right panel of Fig.3(b)). The removal of trapped air from the column demonstrates the existence of an underlying dynamical transition via which the failure-mode transforms from being brittle to being ductile, both of which are collective (multi-particles) in nature, and finally to a total disintegration of the *skin* that represents failure at the single-particle level. This is analogous to dynamical transitions from collective response to single-particle response in a wide class of systems [49].

CONCLUSION

This paper provides a detailed study of mechanical properties of underwater granular structures made of hydrophobic sand, where the self-generated cohesive *skin* on the boundary of the structure encapsulates the dry grains inside it from the surrounding medium water. In our experimental results, three distinct length scales of the system are found. (i) The scale of the hydrophobic patches $\approx \mathcal{O}(1 \mu\text{m})$ influences the strength of the pinning of air-water interface on the grain surfaces. Depinning of this interface produces macroscopically observable plastic deformations of the contact lines around (ii) the grain-scale $\approx \mathcal{O}(10^2 \mu\text{m})$ of the sand particles. (iii) At the sys-

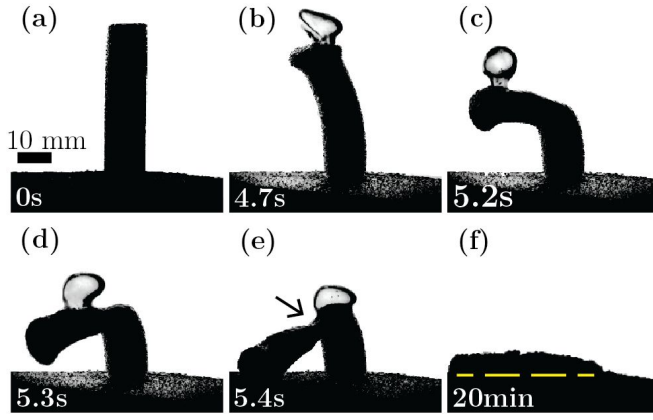


FIG. 9. A sequence of images: (a)→(e) shows an upright sand column ($d = 14$ mm and $L = 50$ mm) which fails in a ductile manner. This mode of failure is initiated by degassing the column and achieved by maintaining a low vacuum state over the free surface of water. The degassing proceeds by emanating bubbles from the column, which reduces the pressure inside the column and thereby forcing conformational changes on the *skin*. (f) The column loses its integrity by the slightest mechanical disturbance and the structure disintegrates into a heap of particles under water.

tem scale $\approx \mathcal{O}(10^4 \mu\text{m})$, the compressive traction forces due to the column's own weight drives the wrinkling of the *skin*. The regions of large curvature of the structure are the seeds from where the system-sized failure modes nucleate. By partially removing the trapped air from this structure, we also see that the collective failure can be tuned from brittle to ductile. A more complete removal of air causes the *skin* to crumble completely into individual non-cohesive grains inside water. These experimental findings imply the existence of a tunable dynamical transition between a collective and an individual (single-grain) mode of failure in this system. We expect that these new results will help in engineering the granular encapsulation with desired material-properties in a variety of applications and, at the same time, it provides a deeper insight of the multi-scale mechanics, generic to granular materials.

We acknowledge discussions with A. Ghatak, M. Tirumkudulu, I. Sharma and M. Bandi. We especially thank the anonymous referees for many critical and valuable comments on the manuscript.

-
- [1] Y. Amarouchene, J.-F. Boudet, and H. Kellay, *Physical Review Letters* **100**, 218001 (2008).
 - [2] X. Cheng, G. Varas, D. Citron, H. M. Jaeger, and S. R. Nagel, *Physical Review Letters* **99**, 188001 (2007).
 - [3] Y. Forterre and O. Pouliquen, *Annual Review of Fluid Mechanics* **40**, 1 (2008).
 - [4] X. Cheng, L. Xu, A. Patterson, H. M. Jaeger, and S. R.

- Nagel, *Nature Physics* **4**, 234 (2008).
- [5] P. G. deGennes, *Reviews of Modern Physics* **71**, S374 (1999).
- [6] S. Strauch and S. Herminghaus, *Soft Matter* **8**, 8271 (2012).
- [7] N. Mitarai and F. Nori, *Advances in Physics* **55**, 1 (2006).
- [8] F. Soulié, F. Cherblanc, M. El Youssofi, and C. Saix, *International Journal for Numerical and Analytical Methods in Geomechanics* **30**, 213 (2006).
- [9] S. Herminghaus, *Advances in Physics* **54**, 221 (2005).
- [10] G. Gutiérrez, C. Colonnello, P. Boltzenhagen, J. R. Darias, R. Peralta-Fabi, F. Brau, and E. Clément, *Phys. Rev. Lett.* **114**, 018001 (2015).
- [11] C. Py, P. Reverdy, L. Doppler, J. Bico, B. Roman, and C. N. Baroud, *Physical Review Letters* **98**, 156103 (2007).
- [12] J. D. Paulsen, V. Démery, C. D. Santangelo, T. P. Russell, B. Davidovitch, and N. Menon, *Nature materials* **14**, 1206 (2015).
- [13] P. Aussillous and D. Quéré, *Nature* **411**, 924 (2001).
- [14] B. P. Binks and S. O. Lumsdon, *Langmuir* **17**, 4540 (2001).
- [15] A. D. Dinsmore, M. F. Hsu, M. G. Nikolaidis, M. Marquez, A. R. Bausch, and D. A. Weitz, *Science* **298**, 1006 (2002).
- [16] M. D. Dickey, R. C. Chiechi, R. J. Larsen, E. A. Weiss, D. A. Weitz, and G. M. Whitesides, *Advanced Functional Materials* **18**, 1097 (2008).
- [17] P. Aussillous and D. Quéré, in *Proceedings of the Royal Society of London A: Mathematical, Physical and Engineering Sciences*, Vol. 462 (The Royal Society, 2006) pp. 973–999.
- [18] M. Abkarian, S. Protière, J. M. Aristoff, and H. A. Stone, *Nature communications* **4**, 1895 (2013).
- [19] A. B. Subramaniam, M. Abkarian, L. Mahadevan, and H. A. Stone, *Langmuir* **22**, 10204 (2006).
- [20] M. Pakpour, M. Habibi, P. Moller, and D. Bonn, *Scientific Reports* **2**, 5498 (2012).
- [21] D. Hornbaker, R. Albert, I. Albert, A.-L. Barabási, and P. Schiffer, *Nature* **387**, 765 (1997).
- [22] K. Saleh and P. Guigon, in *Granulation*, Handbook of Powder Technology, Vol. 11, edited by M. H. A.D. Salman and J. Seville (Elsevier Science B.V., 2007) pp. 323 – 375.
- [23] B. Andreotti, Y. Forterre, and O. Pouliquen, *Granular media: between fluid and solid* (Cambridge University Press, 2013).
- [24] S. Moulinet, C. Guthmann, and E. Rolley, *The European Physical Journal E* **8**, 437 (2002).
- [25] D. Quéré, *Reports on Progress in Physics* **68**, 2495 (2005).
- [26] D. Quéré, A. Lafuma, and J. Bico, *Nanotechnology* **14**, 1109 (2003).
- [27] C. Miguel and M. Rubi, *Jamming, yielding, and irreversible deformation in condensed matter*, Vol. 688 (Springer, 2006).
- [28] A. Varshney, A. Sane, S. Ghosh, and S. Bhattacharya, *Physical Review E* **86**, 031402 (2012).
- [29] G. E. Davis, *Journal of the Optical Society of America* **45**, 572 (1955).
- [30] P. L. Marston, *Journal of the Optical Society of America* **69**, 1205 (1979).
- [31] L. Rondon, O. Pouliquen, and P. Aussillous, *Physics of Fluids* **23**, 073301 (2011).
- [32] P. L. du Noüy, *The Journal of general physiology* **7**, 625

- (1925).
- [33] P. G. de Gennes, *Rev. Mod. Phys.* **57**, 827 (1985).
 - [34] G. Varieschi and K. Kamiya, *American Journal of Physics* **71**, 1025 (2003).
 - [35] R. M. Sutton, *Science* **84**, 246 (1936).
 - [36] P. C. Møller and D. Bonn, *Europhysics Letters* **80**, 38002 (2007).
 - [37] L. Mahadevan and J. B. Keller, *Proceedings of the Royal Society of London A: Mathematical, Physical and Engineering Sciences*, **452**, 1679 (1996).
 - [38] S. Timoshenko, *Theory of Elastic Stability 2e* (Tata McGraw-Hill Education, 1970).
 - [39] J. Hutchinson and W. Koiter, *Appl. Mech. Rev* **23**, 1353 (1970).
 - [40] T. Weinhart, R. Hartkamp, A. R. Thornton, and S. Ludwig, *Physics of Fluids* **25**, 070605 (2013).
 - [41] A. Trujillo-Pino, K. Krissian, M. Alemán-Flores, and D. Santana-Cedr s, *Image and Vision Computing* **31**, 72 (2013).
 - [42] G. Hunt, G. J. Lord, and M. A. Peletier, *Discrete and Continuous Dynamical Systems Series B* **3**, 505 (2003).
 - [43] W. Abramowicz and N. Jones, *International Journal of Impact Engineering* **19**, 415 (1997).
 - [44] J. Barker, D. Schreiber, B. Huth, and D. Everett, in *Proceedings of the Royal Society of London A: Mathematical, Physical and Engineering Sciences*, Vol. 386 (The Royal Society, 1983) pp. 251–261.
 - [45] G. Combe and J.-N. Roux, *Physical Review Letters* **85**, 3628 (2000).
 - [46] S. Karmakar, E. Lerner, and I. Procaccia, *Physical Review E* **82**, 055103 (2010).
 - [47] D. Dyson, *Physics of Fluids (1958-1988)* **31**, 229 (1988).
 - [48] S. D. Antolovich and R. W. Armstrong, *Progress in Materials Science* **59**, 1 (2014).
 - [49] A. Varshney, P. Sharma, A. Sane, S. Ghosh, and S. Bhattacharya, *Phys. Rev. Lett.* **105**, 154301 (2010).